Why intracellular electrodes converge to the microscale

Donhee Ham

donhee@seas.harvard.edu

Harvard University https://orcid.org/0000-0001-6925-2466

Hefei Liu

Harvard University

Yuchang Zhang

Harvard University

Woo-Bin Jung

Pohang University of Science and Technology

Analysis

Keywords:

Posted Date: June 23rd, 2026

DOI: https://doi.org/10.21203/rs.3.rs-10107672/v1

Additional Declarations: There is **NO** Competing Interest.

Why intracellular electrodes converge to the microscale

Hefei Liu[1,&], Yuchang Zhang[1,&], Woo-Bin Jung[1,2,*], and Donhee Ham[1,*]

[1]John A. Paulson School of Engineering and Applied Sciences, Harvard University, Cambridge, MA, USA
[2]Department of Chemical Engineering, Pohang University of Science and Technology, Pohang, South Korea

[&]These authors contributed equally
[*]Corresponding authors: E-mail - donhee@seas.harvard.edu, woobinjung@postech.ac.kr

Nanoscale structures have long been pursued for intracellular recording on the premise that smaller electrodes couple more intimately with cells. This vision animated two decades of nano-bio research in electrophysiology, yet experimental reality has told a different story. Robust intracellular recording in neurons, with reliable subthreshold sensitivity, has remained elusive at the nanoscale; where it has been clearly achieved, the effective electrode dimension has been microscale. Here we show that an optimal electrode size arises intrinsically in intracellular recording, from the competition between electrical physics and probabilistic cell-electrode geometry. We then formalize this competition by extending the standard cell-electrode interface model into a generalized probabilistic model that captures both physics and geometry. This model yields an optimum in or near the microscale range under realistic conditions, accounting for the historical convergence toward microscale electrodes. It also provides a practical basis for analyzing and designing intracellular interfaces.

Intracellular neuronal recording provides access to subthreshold synaptic signals at the core of neural computation, yet remains challenging. Nanoscale electrodes have been extensively explored for intracellular recording on the premise that smaller electrodes could couple more intimately with cells[1-8]. In practice, however, robust intracellular recording in neurons—especially with subthreshold sensitivity—has remained elusive with nanoscale electrodes[5-8]. When achieved, such recording has occurred either through multiple nanostructures electrically short-circuited to operate as an effective microscale electrode[9], or through explicit microscale electrodes[10,11]. It is these microscale electrodes that have enabled routine intracellular recording and, in arrayed form, population-scale intracellular recordings across thousands of neurons, establishing the intracellular microelectrode array (iMEA)[11]. This history suggests electrode size as a fundamental parameter in intracellular recording.

Here we show that electrode size governs intracellular recording through two competing constraints, and that an optimal electrode size emerges from that competition. At small sizes, electrode impedance rises, attenuating signal transfer from the neuron to the measurement electronics (amplifier). At large sizes, full coverage of the electrode by a single cell becomes less probable, diluting the signal from the cell. These opposing penalties must give rise to an optimum in electrode size.

To quantify this optimal behavior and provide a practical framework, we construct a cell-electrode interface model that extends the conventional model by making the two constraints explicit: the electrical physics of signal transfer and the probabilistic geometry of cell-electrode coverage. From this model, a nonmonotonic dependence of intracellular coupling on electrode size emerges, along with an optimal size that, under realistic conditions, falls in or near the microscale range. This establishes the microscale electrode as the practical regime for intracellular recording, consistent with the historical convergence toward the microscale. This framework does not rule out nanoscale operation, but clarifies the conditions required for it and, more broadly, offers guidance for designing intracellular interfaces.

Competing constraints in electrode size. A cell-electrode interface comprises three regions: the interior of the cell, a thin electrolyte layer outside the cell membrane at the electrode interface (the junctional solution), and the electrode[12] (Fig. 1a). Electrical signals inside the cell traverse this layered structure before they are detected at the electrode. Specifically, the voltage inside the cell, V_m, propagates across the membrane to modulate the potential V_s in the junctional solution, which is then sensed by the electrode as a voltage V_e. This signal transfer, $V_m \rightarrow V_s \rightarrow V_e$, is inherently attenuative. The coupling strength, $\alpha \equiv V_e/V_m$

< 1, therefore provides a natural measure of cell-electrode interface. In fact, α is the most fundamental parameter of the interface, directly reflecting how well signal fidelity is preserved. Once the signal reaches the electrode as V_e, it undergoes measurement—namely, amplification. The measurement electronics (an amplifier) inevitably operates with a finite noise floor. Attenuation by α therefore carries a direct penalty: it reduces the signal before amplification, making it more susceptible to corruption by the amplifier noise floor. Maximizing α thus not only preserves as much of the signal as possible, but also minimizes corruption by noise. Maximizing α—minimizing attenuation—before the first stage of amplification is therefore essential. This principle is universal: losses before front-end amplification must be minimized for any sensitive measurement.

Intracellular recording maximizes α by reducing the membrane barrier—via permeabilization or penetration—thus enhancing the $V_m \rightarrow V_s$ step. However, even after the membrane barrier is lowered, α can be severely reduced at either extreme of electrode size.

At very small sizes, the electrode-electrolyte interface impedance Z_e—hereafter referred to simply as the electrode impedance—becomes large, reducing α by attenuating the $V_s \rightarrow V_e$ transfer. This attenuation is governed by the voltage-divider relation, $V_e/V_s = Z_a/(Z_a + Z_e)$, where Z_a is the amplifier input impedance (Fig. 1a). If Z_a were infinite, $V_e/V_s = 1$ for any Z_e or electrode size. In reality, however, Z_a is far from infinite because the elements that define the amplifier input—typically capacitors or transistors—must be of sufficient size to achieve adequate amplifier performance (*e.g.*, gain and noise). Their size introduces non-negligible intended or parasitic capacitances, making Z_a finite and constraining it in practice to a relatively narrow, technologically mature range. Once Z_e exceeds this practical Z_a with electrode downsizing, the division factor V_e/V_s—and thus α—collapses. This limitation reflects a fundamental aspect of measurement: the outcome of measurement cannot be decoupled from the apparatus that performs it.

At very large sizes, the probability of full electrode coverage by a single neuron becomes increasingly small. Under partial coverage, the electrode inevitably straddles the target cell region (junctional solution) and its surroundings—whether bulk solution or neighboring cells. Effectively, the electrode is not fully committed to the junctional solution but has an electrical leakage to the surroundings. This lowers V_e, leading to a marked reduction in α.

These opposing limits—one set by the electrical physics of signal transfer, the other by the probabilistic geometry of cell-electrode coverage—constitute a fundamental trade-off. Electrode size cannot be pushed arbitrarily in either direction without incurring a penalty. This trade-off must give rise to an optimal electrode size.

Probabilistic modeling of the cell-electrode interface. To make the trade-off—and the existence of an optimal electrode size—explicit, we evaluate the coupling strength α as a function of electrode size using a circuit model of the cell-electrode interface. While a circuit-modeling approach would naturally build in the electrical physics of signal transfer, the probabilistic geometry of cell-electrode coverage must be deliberately added. The classical model (Fig. 1a) is limited in this regard because it assumes complete coverage of an electrode by a single neuron and therefore neglects the general case of partial coverage. In this classical picture, the separation between the target cell region (junctional solution) and the surrounding bulk solution is represented solely by the seal resistance R_s, which models imperfect mechanical constriction between the cell membrane and substrate[13].

Figure 1b presents a generalized circuit model that explicitly incorporates partial coverage. The straddling of the junctional solution and the surrounding medium is captured by partitioning the total electrode impedance Z_e into Z_e/f and $Z_e/(1-f)$, where $f \leq 1$ denotes the fraction of electrode area coupled to the junctional solution beneath a cell, and $1–f$ denotes the remainder exposed to the surrounding medium. The classical full-coverage model (Fig. 1a) is recovered as the special case $f = 1$. This generalized framework in Fig. 1b therefore accounts for imperfect separation between the junctional solution and the surrounding medium, arising not only from imperfect mechanical sealing (captured by R_s) but also from imperfect electrical

sealing (captured by f) due to partial coverage, with the latter depending on electrode size. Importantly, f is a random variable: for an electrode of general size—whether implemented singly or in an array, and whether *in vivo* or *in vitro*—the position of a neuron relative to the electrode is random, making partial coverage inherently probabilistic.

With this generalized framework (Fig. 1b) in place, we can now quantify α as a function of electrode size. To treat f probabilistically, we consider a representative geometry that preserves the essence of cell-electrode coverage (Fig. 2a): neurons are modeled as disks of diameter D arranged in a two-dimensional hexagonal close-packed lattice, and the electrode is modeled as a planar disk of diameter d. For a given electrode diameter d, we repeat random placements of the electrode relative to the cell lattice. Each random placement gives a random value of f between the electrode and the nearest neuron, and this value of f is used in the cell-electrode interface model of Fig. 1b to calculate the corresponding α. The repetition of random placements for the same d then yields an ensemble of f values and a corresponding ensemble of α values. The means of these ensembles, $\langle f \rangle$ and $\langle \alpha \rangle$, are the average coverage and average coupling strength for the given d, respectively. Repeating this procedure for different values of d yields $\langle f \rangle$ and $\langle \alpha \rangle$ as functions of electrode size.

Emergence of an optimum: Figure 2b (blue) shows the calculated $\langle \alpha \rangle$ as a function of electrode diameter d for a typical mammalian neuron size (D = 20 μm), using representative values for the model parameters in Fig. 1b[12] and assuming the inverse-area scaling of $Z_e \propto 1/d^2$. The curve exhibits a clear nonmonotonic behavior—the hump—with a maximum. This reflects the aforementioned competing effects that emerge across electrode sizes. At small sizes, $\langle \alpha \rangle$ is limited by large electrode impedance, whereas at large sizes it is limited by partial coverage. The optimal diameter for the maximum $\langle \alpha \rangle$ lies between these limits. More specifically, as electrode size initially increases, $\langle \alpha \rangle$ improves due to the reduction in electrode impedance while the mean coverage $\langle f \rangle$ remains near unity. Beyond a certain size, however, partial coverage becomes dominant and $\langle f \rangle$ decreases, leading to a reduction in $\langle \alpha \rangle$. The optimal electrode size lies in the microscale range.

The large-size limit, set by probabilistic coverage geometry, is dictated by cell size, whereas the small-size limit is governed by the sharp rise of electrode impedance. As a result, varying the electrode's specific impedance (MΩ·μm^2)—a size-independent material/surface parameter—over a wide range based on experimentally reported values from the literature (Fig. 2b, purple and light blue) does not substantially shift the location of the optimum; the optimum remains in or near the microscale range. This overall picture remains unchanged even when the scaling law of Z_e is altered. Figure 2c shows results for $Z_e \propto 1/d$, an alternative scaling motivated by small-electrode electrochemistry[14-16]. Although the dependence on size is softened, the hump persists and the optimum remains in or near the microscale range in all cases.

Power and limitations of three-dimensional electrode shaping: Three-dimensional shaping of electrodes can partially decouple electrode impedance from coverage probability. Extending an electrode into the third dimension increases its surface area—and thus reduces impedance—without increasing its lateral footprint, leaving $\langle f \rangle$ unchanged. A hole electrode exemplifies this principle[11]: for a given lateral footprint, it gains additional surface area through its sidewalls, reducing impedance without any coverage penalty. This is illustrated in Fig. 2d, which compares $\langle \alpha \rangle$ vs. lateral diameter for a hole electrode (red; depth 2 μm) and a planar disk electrode (blue), assuming that Z_e scales inversely with electrode surface area and using a nominal specific electrode impedance. For a given small lateral diameter ($\langle f \rangle \sim 1$) where electrode impedance is the primary determinant of $\langle \alpha \rangle$, the hole outperforms due to its larger surface area. For a given large lateral diameter where $\langle f \rangle$ becomes the primary determinant of $\langle \alpha \rangle$, both geometries yield similar $\langle \alpha \rangle$ as they share the same $\langle f \rangle$. Between these limits, the peak $\langle \alpha \rangle$ shifts to a smaller lateral diameter and reaches a higher value for the hole electrode. Practical constraints, such as achievable hole depth, prevent full decoupling, and the shift in peak $\langle \alpha \rangle$ toward smaller lateral diameters remains bounded. And even where such a shift occurs, the electrode at the shifted peak—measured by total surface area rather than lateral footprint

alone—remains in or near the microscale range. Three-dimensional electrode shaping can partially relax the impedance-coverage trade-off to enhance intracellular coupling, but cannot eliminate it.

Of note, in the calculations of Fig. 2d, the same seal resistance R_s is used for the hole and planar electrodes, even though three-dimensional topography can enhance mechanical sealing and thus further increase $\langle\alpha\rangle$ for the hole electrode. This choice makes clear how three-dimensional shaping relaxes the impedance-coverage trade-off, independent of additional topographic advantages. Protruding structures, such as pillars, similarly increase the electrode surface area and reduce impedance for a given lateral diameter, while also altering the topography of the cell-electrode interface. To date, however, the most robust demonstrations of intracellular recording have been achieved with hole electrodes[11].

Deep-nanoscale penetration limit: As discussed earlier, the drop of $\langle\alpha\rangle$ in the deep-nanoscale regime, on the far-left side of the humps in Fig. 2b and 2c, originates from attenuation in the $V_s \rightarrow V_e$ transfer governed by the voltage divider, $V_e/V_s = Z_a/(Z_a + Z_e)$. In this regime, the small electrode makes Z_e large enough to readily exceed any practical amplifier input impedance Z_a, driving the voltage divider—and thus α—to small values. This is the fundamental size penalty.

The results in Fig. 2b and 2c assume a residual membrane barrier at a level expected for permeabilization-mediated intracellular access. The original motivation for deep-nanoscale electrodes in the nano-bio literature was the possibility—however challenging—of achieving membrane penetration, which would reduce the membrane-side attenuation beyond what permeabilization provides. Such membrane penetration would thus elevate α relative to the values in Fig. 2b and 2c in the deep-nanoscale regime. Whether the elevated α would become practically high enough is uncertain and depends on technical details. That possibility—difficult as it may be—would at least become more likely if the baseline deep-nanoscale size penalty set by the $V_s \rightarrow V_e$ voltage divider, $Z_a/(Z_a + Z_e)$, were made less severe, either by reducing the electrode's specific impedance below typical values or by increasing Z_a beyond its practical range. Both routes, however, are non-trivial in practice.

Reducing the electrode's specific impedance is non-trivial at deep-nanoscale dimensions, where conventional surface-roughening has little room to operate because the electrode itself is comparable in size to roughening features (*e.g.*, platinum black particles).

Increasing Z_a beyond a practical range is equally non-trivial. Amplifiers typically feature capacitors or transistors at their input, from which Z_a arises through their intended or parasitic capacitances. To ensure adequate amplifier gain and noise performance, these input elements must be of sufficient size, which prevents Z_a from being arbitrarily increased. Attempts to excessively increase Z_a degrade amplifier performance and yield no net benefit. For example, consider an amplifier featuring a transistor at its input, through which the deep-nanoscale electrode interfaces (Fig. 3a). The transistor sets the amplifier gain via its transconductance g_m and sets Z_a via its parasitic capacitance. Reducing the effective size of the transistor—and hence its parasitic capacitance—increases Z_a, thereby improving $Z_a/(Z_a + Z_e)$ and consequently α. Such transistor downscaling, however, reduces g_m and hence amplifier gain. Thus, input-transistor downscaling leaves the overall gain of the electrode-amplifier chain, proportional to αg_m, without net improvement (once the amplifier itself is modified, not only α but αg_m must be considered). The same conclusion applies to signal-to-noise ratio as well. This exemplifies that increasing Z_a does not salvage the nanoscale electrode. Nanoscale electrodes may overcome the membrane, but cannot overcome the physics of measurement governed here by the voltage divider.

Beyond passive electrodes: The physics of measurement cannot be escaped—but the voltage divider within it can, by shifting the deep-nanoscale interface from passive to active. So far, our analysis has remained within a passive-electrode architecture, the dominant approach in electrophysiology: the electrode transduces the signal, and a separate amplifier detects it. The foregoing discussion around Fig. 3a was an instance of this passive architecture in the deep-nanoscale penetration limit: the electrode-electrolyte interface impedance Z_e was unavoidable, and the voltage divider $Z_a/(Z_a + Z_e)$ was inescapable.

The shift to the active route escapes the voltage divider by eliminating Z_e altogether. This active approach places a deep-nanoscale semiconductor within the cell and uses it as a transistor channel directly gated by the intracellular electrolyte, without a passive electrode[17] (Fig. 3b). Thus $Z_e = 0$, so $Z_a/(Z_a + Z_e) = 1$, effectively eliminating the voltage divider. Here, the transistor is made nanoscale so that it can reside within the cell and form the active interface; as a result, its transconductance g_m is small. However, because α is fixed *a priori* at its maximal value of 1, the trade-off between α and g_m seen in the passive electrode architecture is side-stepped. This suggests that the deep nanoscale may be better suited to active interfaces than to passive electrodes.

Conclusion

The premise that smaller electrodes couple more intimately with cells and may more readily cross the membrane has been a natural and productive driver of nano-bio research in electrophysiology. That intuition captured an important part of the problem, but not the whole of it. Intracellular recording is not a one-directional scaling problem. It is an optimization problem shaped by the interplay between the physics of electrical signal transfer (including measurement) and cell-electrode geometry. In fact, robust, routine intracellular recording with subthreshold sensitivity has been achieved by microscale electrodes. The framework developed here shows that an optimum electrode size emerges for intracellular recording, and that it lies in or near the microscale range under realistic conditions, consistent with the historical trajectory of the field. At the same time, this framework neither argues against the nanoscale nor closes the door to it. Rather, it clarifies what nanoscale approaches must overcome, however challenging. The framework provides a quantitative basis for evaluating such efforts and for guiding the design of intracellular interfaces more broadly.

Methods

Generalized probabilistic cell-electrode interface model. We model the cell-electrode interface with the generalized circuit shown in Fig. 1b. It comprises the junctional membrane impedance Z_{jm}, the seal resistance R_s, the amplifier input impedance Z_a, and the electrode-electrolyte interface impedance Z_e (hereafter the electrode impedance). To account for partial coverage of the electrode by a single target cell, the total electrode impedance Z_e is partitioned into $Z_{e,f} \equiv Z_e/f$ and $Z_{e,(1-f)} \equiv Z_e/(1-f)$, where $f \leq 1$ is the fraction of the electrode area coupled to the junctional solution beneath the target cell and $1-f$ is the fraction exposed to the surrounding medium, which may include bulk solution or neighboring cells. For a given f, the coupling strength $\alpha = V_e/V_m$ calculated from this circuit is given by

$$\alpha = \frac{R_s || Z_{in,e}}{R_s || Z_{in,e} + Z_{jm}} \cdot \frac{Z_a || Z_{e,(1-f)}}{Z_a || Z_{e,(1-f)} + Z_{e,f}} \qquad (1)$$

where $Z_{in,e} \equiv Z_{e,f} + Z_a \,||\, Z_{e,(1-f)}$. The classical full-coverage model (Fig. 1a) is recovered as the special case $f = 1$. For a given f, α is determined through Eq. (1). Because f is a random variable, each value of f yields a corresponding α. The ensemble average $\langle\alpha\rangle$ is then the mean of these individual α values corresponding to the distribution of f.

Monte Carlo sampling of the coverage geometry. Neurons are modeled as identical disks of diameter $D = 20$ µm arranged in a two-dimensional hexagonal close-packed lattice, and the electrode as a planar disk of variable diameter d. To obtain the distribution of f for an electrode with a given d, the electrode is placed at $N = 10{,}201$ random positions within a single repeating unit of the lattice, exploiting its periodicity. For each placement, the overlap fraction f between the electrode and the nearest neuron is computed as the ratio of overlap area to total electrode area, with this nearest neuron taken as the target cell. The 10,201 resulting values of f yield 10,201 values of α through Eq. (1), whose mean is $\langle\alpha\rangle$. This procedure is repeated for d spanning 2 nm to 60 µm, at 25 logarithmically spaced points per decade, giving $\langle\alpha\rangle$ as a function of electrode size.

Model parameters and electrode impedance scaling. Unless otherwise stated, we set $Z_a = 50$ MΩ, $R_s = 100$ MΩ, and $Z_{jm} = 400$ MΩ, all evaluated at 1 kHz, with Z_{jm} corresponding to a level expected for permeabilization-mediated intracellular access[12]. Z_e scales with electrode size, and we consider two limiting cases: inverse scaling with area, or with a linear dimension. For a planar disk electrode of diameter d, we examine both: $Z_e \propto 1/d^2$ (Fig. 2b) and $Z_e \propto 1/d$ (Fig. 2c). In each case the proportionality constant is set by the electrode's specific impedance, taken over a range spanning experimentally reported values: 500, 50, 5 MΩ·µm^2 for Fig. 2b and 125, 25, 5 MΩ·µm for Fig. 2c. For the 2-µm deep hole electrode (Fig. 2d), we show only area scaling, now applied to its full three-dimensional surface, using the nominal specific impedance of 50 MΩ·µm^2; the linear dimension scaling follows the same logic and is not repeated.

Software Calculations were performed in MATLAB R2025b. See Code Availability.

REFERENCES

1 Xie, C., Lin, Z., Hanson, L., Cui, Y. & Cui, B. Intracellular recording of action potentials by nanopillar electroporation. *Nature Nanotechnology* **7**, 185-190 (2012).

2 Abbott, J. *et al.* CMOS nanoelectrode array for all-electrical intracellular electrophysiological imaging. *Nature Nanotechnology* **12**, 460-466 (2017).

3 Desbiolles, B. X. E., de Coulon, E., Bertsch, A., Rohr, S. & Renaud, P. Intracellular recording of cardiomyocyte action potentials with nanopatterned volcano-shaped microelectrode arrays. *Nano Letters* **19**, 6173-6181 (2019).

4 Jahed, Z. *et al.* Nanocrown electrodes for parallel and robust intracellular recording of cardiomyocytes. *Nature communications* **13**, 2253 (2022).

5 Liu, R. *et al.* Ultra-sharp nanowire arrays natively permeate, record, and stimulate intracellular activity in neuronal and cardiac networks. *Advanced Functional Materials* **32**, 2108378 (2022).

6 Robinson, J. T. *et al.* Vertical nanowire electrode arrays as a scalable platform for intracellular interfacing to neuronal circuits. *Nature Nanotechnology* **7**, 180-184 (2012).

7 Liu, R. *et al.* High density individually addressable nanowire arrays record intracellular activity from primary rodent and human stem cell derived neurons. *Nano Letters* **17**, 2757-2764 (2017).

8 Tchoe, Y. *et al.* A scalable fishbone nanowire array (FINE) for 3D quasi-Intracellular recording in intact brains. *Advanced Materials* **37**, e04171 (2025).

9 Abbott, J. *et al.* A nanoelectrode array for obtaining intracellular recordings from thousands of connected neurons. *Nature biomedical engineering* **4**, 232-241 (2020).

10 Hai, A., Shappir, J. & Spira, M. E. Long-term, multisite, parallel, in-cell recording and stimulation by an array of extracellular microelectrodes. *Journal of Neurophysiology* **104**, 559-568 (2010).

11 Wang, J., Jung, W.-B., Gertner, R. S., Park, H. & Ham, D. Synaptic connectivity mapping among thousands of neurons via parallelized intracellular recording with a microhole electrode array. *Nature biomedical engineering* **9**, 1144-1154 (2025).

12 Abbott, J. *et al.* The design of a CMOS nanoelectrode array with 4096 current-clamp/voltage-clamp amplifiers for intracellular recording/stimulation of mammalian neurons. *IEEE Journal of Solid-State Circuits* **55**, 2567-2582 (2020).

13 Okada, Y. *Patch clamp techniques*. (Springer, 2012).

14 Newman, J. Resistance for flow of current to a disk. *Journal of the Electrochemical Society* **113**, 501-502 (1966).

15 Wightman, R. M. Microvoltammetric electrodes. *Analytical Chemistry* **53**, 1125A-1134A (1981).

16 Bard, A. J., Faulkner, L. R. & White, H. S. *Electrochemical methods: fundamentals and applications*. (John Wiley & Sons, 2022).

17 Zhao, Y. *et al.* Scalable ultrasmall three-dimensional nanowire transistor probes for intracellular recording. *Nature Nanotechnology* **14**, 783-790 (2019).

DATA AVAILABILITY

The numerical data underlying the figures in this study can be generated from the parameters specified in the manuscript using the code described below.

CODE AVAILABILITY

The custom code in MATLAB R2025b implementing the cell-electrode interface model and Monte Carlo simulations is available from the corresponding authors upon reasonable request.

ACKNOWLEDGEMENTS

We thank N. Talha and S. Fan of Harvard University and J. Wang of Virginia Tech for discussions. We acknowledge support from Samsung Advanced Institute of Technology, Samsung Electronics, Suwon, Republic of Korea (A59707 and A37734 to D.H.) and the Gates Foundation (INV-089977 to D.H.) for research related to this work.

AUTHOR CONTRIBUTIONS

H.L., Y.Z., W-B.J., and D.H. conceived the study. H.L. and Y.Z. performed the modeling and calculations. H.L., Y.Z., W-B.J., and D.H. analyzed the results. H.L., Y.Z., W-B.J., and D.H. wrote the manuscript.

COMPETING INTERESTS

The authors declare no competing interests.

ADDITIONAL INFORMATION

Correspondence should be addressed to D.H. and W-B.J.

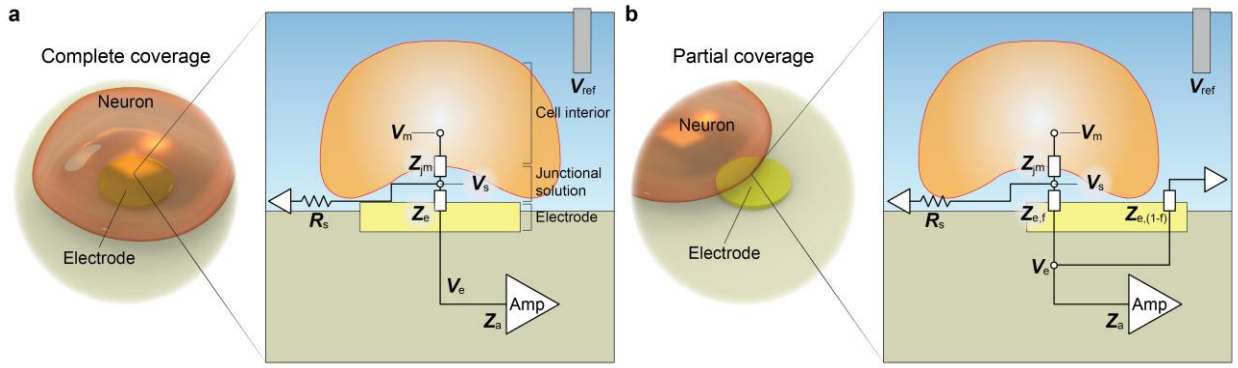

Fig. 1 | Classical and generalized circuit models of the cell-electrode interface. a, Classical model. A full coverage of an electrode by a cell is assumed. Z_{jm}, Z_e, and Z_a denote the junctional membrane impedance, electrode impedance, and amplifier input impedance, respectively. The seal resistance R_s provides the only leakage path. **b,** Generalized model. The model incorporates partial coverage of an electrode by a target cell, while subsuming the classical full-coverage case as a special limit ($f = 1$), where f is the fraction of electrode area coupled to the junctional solution beneath the target cell. The electrode region uncovered by the target cell introduces an additional leakage path beyond R_s. The electrode impedance is partitioned into Z_e/f and $Z_e/(1-f)$, corresponding to the covered and uncovered regions, respectively. In the figure, these are denoted as $Z_{e,f}$ and $Z_{e,(1-f)}$.

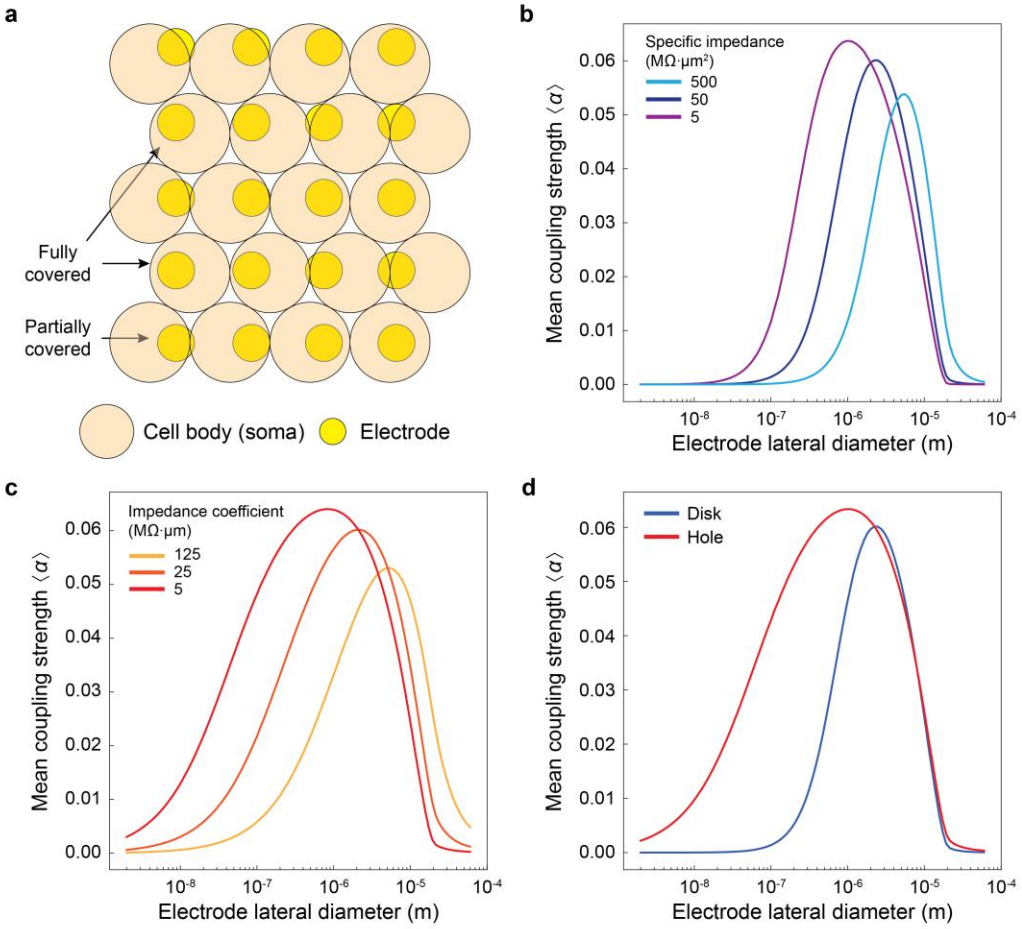

Fig. 2 | Emergence of a microscale optimum. a, Neurons are modeled as disks (diameter D = 20 μm) arranged in a hexagonal close-packed lattice, and the electrode is modeled as a planar disk (diameter d). The electrode is placed at random positions relative to the lattice for Monte Carlo sampling. For each placement, the fractional overlap with the nearest neuron defines f, which is mapped to α via the generalized cell-electrode interface model in Fig. 1b. Repeating this procedure yields ensembles of f and α, from which the means $\langle f \rangle$ and $\langle \alpha \rangle$ are obtained. **b,** $\langle \alpha \rangle$ vs. d for a planar disk electrode, assuming Z_e scaling as $1/d^2$. The three curves correspond to different values of the electrode's specific impedance (MΩ·μm^2), chosen to span experimentally reported values from the literature. **c,** $\langle \alpha \rangle$ vs. d for a planar disk electrode, assuming Z_e scaling as $1/d$. The three curves correspond to different impedance coefficients (MΩ·μm), chosen to span experimentally reported values from the literature. **d,** Comparison of a planar disk electrode and a hole electrode with a fixed depth of 2 μm. In both cases Z_e is assumed to scale inversely with electrode surface area (the area-based scaling as in **b**), using the nominal specific electrode impedance corresponding to the middle curve in **b**. The results in **b**-**d** are obtained by Monte Carlo sampling as described in **a**. For all cases, Z_a = 50 MΩ at 1 kHz is used for the amplifier, while R_s = 100 MΩ and Z_{jm} = 400 MΩ at 1 kHz (with membrane permeabilization) are used for the cell-electrode interface[12].

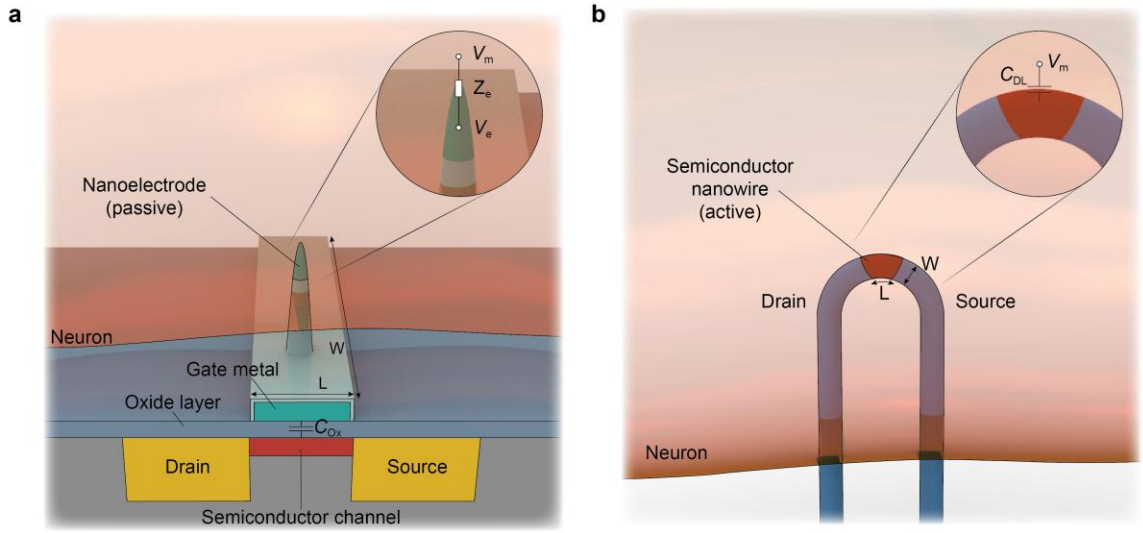

Fig. 3 | The physics of measurement in passive nanoelectrodes and active nanowires. a, In the passive electrode architecture, an electrode transduces the signal, which is detected by a separate amplifier. An illustrative example is shown here: a passive nanoelectrode penetrates a neuronal membrane in the idealized limit ($R_s = \infty$, $Z_{jm} = 0$, $f = 1$), and the subsequent amplifier is implemented with a transistor input. The overall gain of the electrode-amplifier chain is proportional to αg_m, where g_m is the transistor transconductance ($g_m \propto W/L$, with L the transistor channel length and W the channel width). Z_a is also set by the transistor: $Z_a \propto 1/(C_{OX}WL)$ with C_{OX} the gate-oxide capacitance per unit area. The unavoidable electrode-electrolyte interface impedance Z_e enforces a voltage division such that, in the idealized limit shown here, $\alpha = Z_a/(Z_a + Z_e)$. Increasing Z_a through transistor downscaling (reducing W) raises α, but simultaneously reduces $g_m \propto W/L$, leaving the overall gain factor αg_m of the electrode-amplifier chain unimproved. **b,** An active architecture realized by placing a semiconductor nanowire field-effect transistor (channel width W, length L) inside the neuron[17]. The idealized limit ($R_s = \infty$, $Z_{jm} = 0$, $f = 1$) is assumed. The intracellular electrolyte directly—without a passive electrode—gates the transistor channel via the electrical double-layer capacitance (its per-unit area value is denoted as C_{DL}), such that $Z_e = 0$, yielding $\alpha = Z_a/(Z_a + Z_e) = 1$, effectively eliminating the voltage divider. Here Z_a arises from the double-layer capacitance: $Z_a \propto 1/(C_{DL}WL)$. Although the transconductance g_m is small because the transistor is made nanoscale to reside within the cell, α is fixed *a priori* at its maximal value of 1. This removes the trade-off between α and g_m seen in part **a** and raises the possibility of improved signal-to-noise ratio performance relative to passive nanoelectrodes.